Wiley–Society For Biomaterials

Bio-inspired Materials for Biomedical Engineering

Edited By **Anthony B. Brennan & Chelsea M. Kirschner**

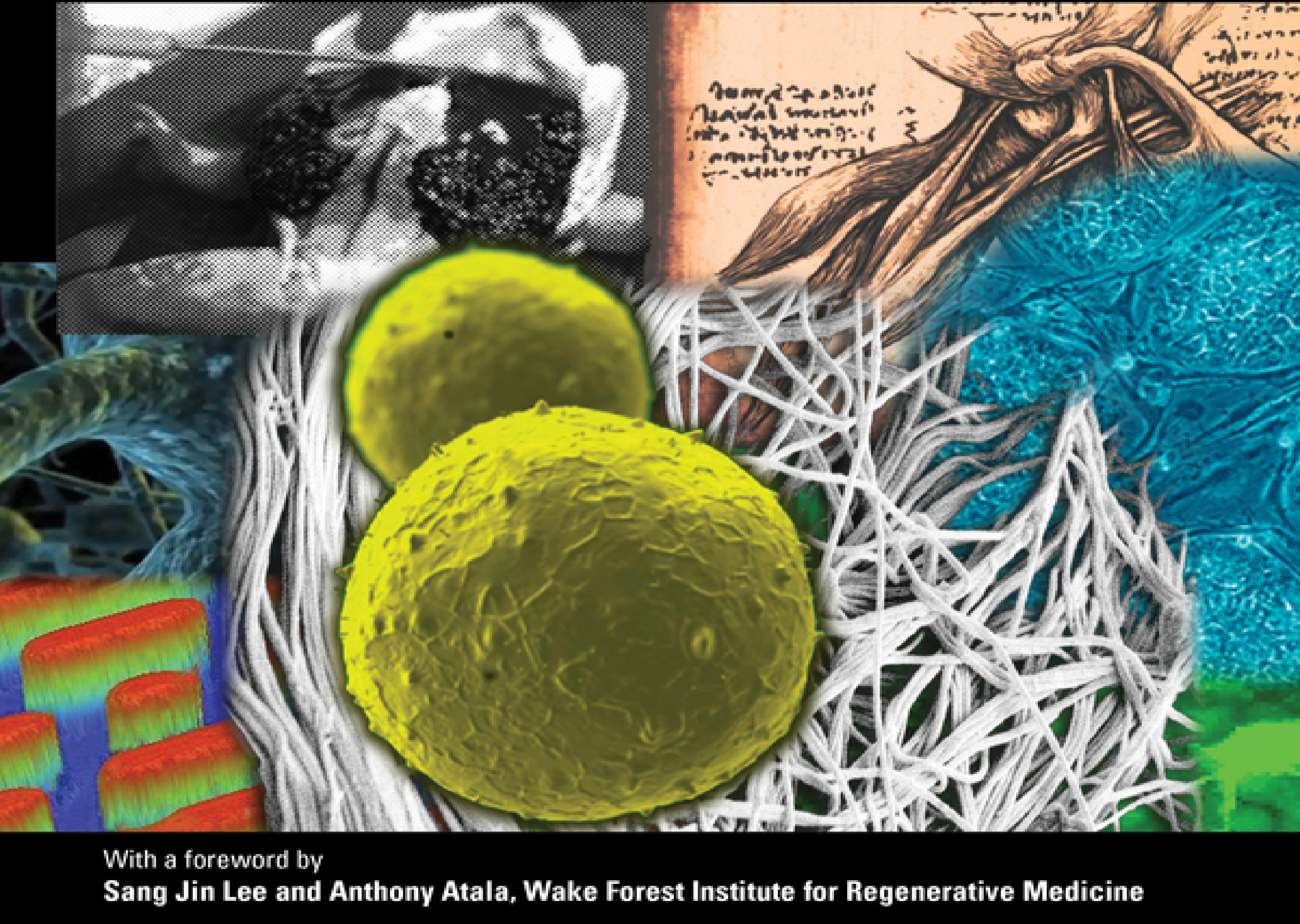

With a foreword by

Sang Jin Lee and Anthony Atala, Wake Forest Institute for Regenerative Medicine

Society For Biomaterials
Giving life to a world of materials

WILEY

Table of Contents

List of Tables

List of Illustrations

function. (Reproduced with permission from Owen, S.C., Shoichet, M.S. *Journal of Biomedical Materials Research A* **2011**, *94A*(4). Copyright 2013 Wiley Periodicals Inc.)

Figure 1.2 Typical orthogonal chemical reactions enable biomaterials to be synthesized with defined chemical and physical properties. Shown are a series of orthogonal *click* reactions which form covalent, irreversible (left panel) [27, 65, 79, 101–106] to near-covalent (middle panel) [63, 65, 107] to reversible (right panel) [52, 69, 70, 108, 109] bonds. For peptide or protein immobilization, this approach results in biomaterials that promote specific cellular responses, such as adhesion, proliferation, migration, and/or differentiation, depending on the biomolecule immobilized.

Figure 1.3 3-D photopatterning of EGF within a hyaluronic acid–PEG hydrogel. (A) Creation of a linear immobilized gradient of EGF. From the top of the hydrogel, the number of scans by the multiphoton laser are increased as it penetrates into the sample, corresponding to an increase in fluorescence intensity, and hence, an increase in protein immobilization. (B) The concentration of immobilized protein in the gradient was quantified by fluorescence intensity, showing a change in concentration from 25 nM at the top of the hydrogel to 250 nM at a depth of 150 μm in the hydrogel. EGF, epidermal growth factor. (Reproduced with permission from Owen, S.C., Fisher, S.A., Tam, R.Y., Nimmo, C.M., Shoichet, M.S. *Langmuir* **2013**. Copyright 2013 American Chemical Society.) *(See insert for color representation of the figure.)*

Figure 2.1 Range of stiffness from different synthetic and natural polymers. Note that citations in parentheses

rudiment or joint due to abnormal muscle, green indicates no effect, striped red and green indicates findings of affected and unaffected aspects, and white indicates no data available. (Reproduced with permission from Reference 69.) *(See insert for color representation of the figure.)*

Figure 4.1 Molecular pathways mediating mechanotransduction signaling in a cell. In this pathway, mechanical forces such as, stretching, hydrostatic pressure, and shear stress stimulate the integrins on the cell membrane via extracellular matrix. In turn, the stimuli is transduced into the nucleus by engagement of anchorage proteins talin (tal), vinculin (vin), paxillin (pax), and α-actinin and signaling proteins FAK, Src, and zyxin (zyx). *(See insert for color representation of the figure.)*

Figure 4.2 Perfusion scheme designed for culturing cell in interconnected porous scaffolds. A peristaltic pump circulates and purges culture medium into a perfusion chamber where porous scaffolds are placed in a sealed holder. The culture medium is forced through the pores of the scaffold and the perfused medium is collected at the lower side of the chamber to be recycled or disposed.

Figure 4.3 (A) Compression and (B) strain mechanical setups that mimic biomechanics of the scaffolds in bioreactors. In the compression bioreactors, the load cell applies a periodic load on the scaffolds with seeded cells. Similarly, the scaffold cells can be strained periodically in the bioreactor by extending the structure with a gripping load cell.

Figure 5.1 (A) *In vivo* cells receive biochemical and biophysical cues through interactions with the ECM, soluble factors, and neighboring cells. Integrins (pink) in the cell membrane bind to ECM proteins (purple), soluble growth factors (green) bind to surface receptors (blue), and cell–cell junctions are formed with adjacent cells (purple). These signals influence cell function through signaling pathways that involve the cytoskeletal (orange fibers) arrangement and focal adhesion placement. (B) A scanning electron micrograph reveals the complex architecture of the basement membrane of a porcine urinary bladder. The fibrous ECM guides cell shape and function within the tissue. (Courtesy of Christopher Carruthers and Denver Faulk of the Badylak Research Group.) *(See insert for color representation of the figure.)*

Figure 5.2 Schematic of the process of e-beam lithography used to print a photomask from a CAD drawing of a designed pattern. (1) Electron beam source. (2) Electron beam used to print pattern to a photomask. (3) Photoresist-coated photomask.

Figure 5.3 Schematic of the photolithography process used to transfer the pattern on a photomask to a photoresist-coated silicon wafer. (3) Photomask containing a pattern of clear features on a black background. (4) Ultraviolet light source. (5) Photoresist-coated silicon wafer.

Figure 5.4 Etch processing of pattern silicon wafers using deep reactive ion etching. (5) Schematic of a cross-section of a patterned silicon wafer with bare silicon features surrounded by photoresist. Silicon covered in photoresist is not etched during the process. (6) Scanning electron micrograph of the cross-section of an etched silicon wafer showing features within the silicon surface.

Figure 5.5 Designed patterns drawn in AutoCAD®. (A) 10-μm equilateral triangles surrounded by 2-μm

Figure 5.12 Light micrograph image of a rejected sample of an engineered topography on the surface of PDMSe taken during the final pattern fidelity assessment before biological testing. The defects appear as dark spots in the image, indicating that those features had flopped over during fabrication and sample preparation. This is an example of an engineered topography of pattern fidelity of <97%.

Figure 5.13 Light micrograph image of a high-fidelity sample (>99%) of an engineered topography on the surface of PDMSe taken during the final pattern fidelity assessment before biological testing. Unlike in Figure 5.12, no defects are visible within the field of view.

Figure 5.14 Sharklet engineered microtopographies varying in the distinct number of features (n) replicated in PDMSe. (A) +1SK2x2_n1, (B) +1SK2x2_n2, (C) +1SK2x2_n3, (D) +1SK2x 2_n4, (E) +1SK2x2_n5. (F) Average aspect ratio for SMCs cultured on PDMSe Sharklet microtopographies after 24 hours. Significant differences in cell morphology were induced by altering feature geometry and arrangement. Error bars, 95% CI.

Figure 5.15 Fluorescent images of hMSCs labeled with CellTracker™ Green CMFDA (5-chloromethylfluorescein diacetate) (Life Technologies, Grand Island, NY), invitrogen, to track cellular morphology on sequentially presented dynamic microtopographies. hMSCs were first seeded onto smooth surfaces, which were patterned sequentially using photolithography (365 nm, 10 mW/cm^2, 250 seconds) into an anisotropic, channels pattern and then an isotropic, squares pattern *in situ*. Cells exhibited a rounded morphology on the smooth pattern, then on patterning, elongated along the features on the channels topography and returned to a more rounded morphology after presentation of the squares pattern. (Reprinted with permission from Reference 52.)

Figure 6.1 An assembled image of known FN structures. FN is a dimer of two 250-kDa monomers, each of which consists of 30–32 individually folded domains. These domains have one of three structures, referred to as type I, type II, or type III domains. Type I and type II domains have several internal disulfides and, are thus, unlikely to unfold when subjected to cell-derived forces. Type III domains have no internal disulfides, and previous studies have shown that these domains unfold under tension. The schematic shown in the figure represents the entire FN dimer, and is based on protein data base (PDB) files of structures for known domains of FN. The loop in the type III domains shows the interactions, which have been shown to exist in the compact conformation of FN. The RGD binding site, which is often substituted for the full molecule in tissue engineering applications, is contained on a single loop of the 10th type III domain. Compiled image was generated from PDB files: FNI^{1}: 1O9A [94]; FNI$^{2-3}$: 3CAL [95]; FNI$^{4-5}$: 2RL0 [95]; FNI^{6}-II^{1}-II^{2}: 1E88 [96]; FNI$^{8-9}$: 3GXE [97]; FNIII$^{1-2}$: 2HA1 [98]; FNIII$^{7-10}$: 1FNF [15]; FNIII$^{12-14}$: 1FNH [99]. Images for domains without published structures were generated in SPDBViewer (Swiss Institute of Bioinformatics, Basel, Switzerland) by matching the sequence to the structure of the same domain homology (i.e., FNIII$^{3-6}$ was generated by matching AA sequence to FNIII$^{7-10}$ structure).

Figure 6.2 Untwisting of type III domains. Steered Molecular Dynamics (SMD) predicts a stable intermediate in which the beta strands of the type III domains have been straightened and aligned. In the unstretched state, nonspecific beta-strand addition is inhibited by the twisting of the beta strands, while in the stretched state, the beta strands along the domain edges are straightened, allowing for beta-strand addition. This image was made with VMD 1.8.7. software support. VMD (Visual Molecular Dynamics) is developed with NIH support by the Theoretical and Computational Biophysics group at the Beckman Institute, University of Illinois at Urbana–Champaign. NIH, National Institutes of Health.

Figure 6.3 Assembly of FN matrix in hMSCs. Confluent layers of hMSCs assemble extensive FN matrices. (A) F-actin immunofluorescence; (B) FN labeled with anti-cellular FN antibody indicates that assembled FN was expressed in hMSCs; (C) Composite image of cell–matrix interactions. *(See insert for color representation of the figure.)*

Figure 6.4 Assembly of FN matrix on a micropillar scaffold. Immunofluorescence images of a layer of human mesenchymal stem cells grown on a surface of micropillars for 10 days. (A) Fluorescently labeled pillars; (B) Actin cytoskeleton (red) (higher magnification shown in C); (D) Assembled fibronectin fibrils (higher magnification shown in E); (F) Composite image. Note that while there are visible spaces between cells in the actin image, they have formed a complete layer of ECM across the top surface of the pillars. Scale bar is 50 μm. *(See insert for color representation of the figure.)*

Figure 9.1 Application of allogenic product to leg wound. (Courtesy of Lauren R. Bayer, PA-C.) *(See insert for color representation of the figure.)*

Figure 9.2 Schematic of the bilayer device. (Reprinted from Yannas, I.V., Orgill, D.P., Burke, J.F. Template for skin regeneration. *Plastic and Reconstructive Surgery*

127 Suppl 1, 60S–70S, 2011 with permission from Wolters Kluwer Health. Modified from original Yannas, I.V., Burke, J.F., Orgill, D.P., Skrabut, E.M. Wound tissue can utilize a polymeric template to synthesize a functional extension of skin. *Science* **1982**; *215*, 174–176 with permission from the American Association for the Advancement of Science.)

Figure 9.3 A 65-year-old woman treated with resection and application of a dermal regeneration template. The silicone was removed at 1 month and a thick skin graft was taken from the upper arm. At 1 year, there is an excellent color match of the skin. (Reprinted from Yannas, I.V., Orgill, D.P., Burke, J.F. Template for skin regeneration. *Plastic and Reconstructive Surgery* 127 Suppl 1, 60S–70S, 2011 with permission from Wolters Kluwer Health.) *(See insert for color representation of the figure.)*

Figure 10.1 Epithelial morphogenesis. Schematic of various epithelial shapes. (A) Tightly connected epithelial sheet with distinct apical (dotted line) and basal (filled line) polarity. (B) Folded epithelium. (C) Epithelial tube. (D) Branching epithelium.

Figure 10.2 Epithelial morphogenesis during development. (A) Epithelial movement within the enveloping layer (EVL) of the zebrafish embryo. Note that the monolayer of cells moves over the surface of the embryo. (B) Epithelial folding during gastrulation of *Drosophila*. Shown are the adherens junctions (zonula adherens [ZA]), the basal junctions (BJ), and myosin (M). Note the bending of the cells as the ventral furrow forms. (C) Multiple steps of folding, relaxing, and growth of epithelium during optic cup morphogenesis. Shown are Rx-GFP-labeled retinal anlagen, which first appear as the optical vesicle. (D) Neural tube formation during primary neurulation in the chicken embryo. (E) Secondary neurulation in the mouse embryo. (F) Branching morphogenesis of the mouse mammary gland. (G) Branching morphogenesis of the embryonic mouse lung. (Adapted from References 5, 24, 32, 37, 51, 53, and 78.)

Figure 10.3 Engineering approaches that mimic epithelial morphogenesis. (A) Micropatterned adhesive substratum for investigating epithelial sheet migration. (B) Mimicking wounded epithelium using PDMS pillars. (C) Switchable substratum for expansion of epithelial sheets. (D) 3-D printing for constructing a biological tube. (E,F) 3-D micropatterned tubes for investigating branching morphogenesis. (Adapted from References 55, 57, 59, 71, and 72.) *(See insert for color representation of the figure.)*

Figure 11.1 Schematic illustration of the structure of natural skin. Keratinocytes are the most common cells in the epidermis and fibroblasts are the major cellular components of dermis. Compared with the fibroblasts that are embedded in fibrous ECM, keratinocytes rest on a thin ultrafine fibrous membrane called the basement membrane.

Figure 11.2 (A) Schematic depiction of the electrospinning process to obtain random nanofiber meshes. A charged solution is drawn from the tip and the residual random fibers collect on a grounded stationary plate. (B) A spinning disk technique is commonly employed to create aligned electrospun fibers. (C) Random nanofiber meshes collected on a grounded plate. (D) Aligned nanofiber meshes prepared utilizing the spinning disk.

Figure 11.3 A schematic illustration of the on-site layer-by-layer cell assembly while electrospinning. As indicated by different colors, both fiber and cell layers can be varied during the cell assembly to create a customized final 3-D construct according to the design. (Reprinted from Reference 98, with permission from Mary Ann Liebert, Inc. Publishers).

Figure 11.4 H&E-stained cross-sections of bilayer skin tissues composed of epidermal (E) and dermal (D) layers and formed by culturing L-b-L assembled cell/fiber constructs for 3 days (A) and 7 days (B). Green broken line outlines the border between E and D. (Reprinted from Reference 98, with permission from Mary Ann Liebert, Inc. Publishers.) *(See insert for color representation of the figure.)*

Figure 12.1 A schematic of the multiscale hierarchy of the myocardium. The generation of macroscale forces requires a precise architecture spanning eight orders of spatial magnitude from nanometers up to centimeters. Actin–myosin molecular motors are organized as overlapping filaments that are assembled into sarcomeres, which in turn form myofibrils spanning an entire cell. Myocytes are mechanically and electrically coupled via intercalated disks to form multicellular myofibers that are organized into aligned 2-D sheets. The ventricles in the heart are composed of overlapping myocyte sheets forming lamellar-like layers.

Figure 12.2 Myofiber orientation in a rat heart. The orientation of the myofibers was reconstructed by fitting a generalized helicoid model to an MRI dataset. The schematic of the heart shows the three areas of observation (red penetrating arrows) at the base, equator, and apex (clockwise from top right). At each location, the orientation of the myofibers through the myocardium, from endocardium (innermost layer) to the epicardium (outermost) is shown. Myofiber orientation was reconstructed (blue rods) by interpolating orientations obtained from MRI data (red rods). MRI, magnetic resonance imaging. (Reprinted with permission from Reference 141.)

Figure 12.3 Mechanical and structural characteristics of the myocardium. The typical arrangement of aligned myofibers gives the myocardium highly anisotropic tensile properties. (A) A schematic representation of a mammalian heart. (B) Confocal microscopy image of the right ventricular myocardium of an adult rat showing the oriented myofibers, labeled for F-actin (green) and cell nuclei (blue). (C,D) Uniaxial tensile stress–strain plots of right ventricular myocardium along the circumferential and longitudinal direction illustrates the mechanical anisotropy (C, full range to demonstrate failure properties; D, physiologic regime). Scale bar in (B) is 50 μm. CIRC and LONG stand for circumferential and longitudinal axes, respectively. (Reprinted with permission from Reference 18.) *(See insert for color representation of the figure.)*

Figure 12.4 The cardiac conduction system. (A) Representative action potentials for components of the conduction system in the chick heart illustrated in (B). The action potentials originating in the SA node undergo several transformations as they travel through the atria, the AV node, and finally the Purkinje fibers and the ventricles. Panels on the right show the Purkinje fibers (green) within the myocardium (red) at different locations in the ventricles. (C) Subendocardial Purkinje fibers. (D) Branch point from subendocardial Purkinje fibers. (E) Intramural Purkinje fibers. AO, aorta; AV, atrioventricular; LV, left ventricle; RV, right ventricle; SA, sinoatrial. (Reproduced with permission from Reference 26.) *(See insert for color representation of the figure.)*

Figure 12.5 The whole vasculature of an adult rat heart was reconstructed (top left) from micro-CT data (top right). Transverse sections obtained in four planes (below) show the penetrating network of capillaries. The color of the rendered vessels corresponds to the intensity of the voxels in the original dataset. (Reprinted with permission from Reference 142.) *(See insert for color representation of the figure.)*

Figure 12.6 Scanning electron microscopy (SEM) images of porcine myocardium after decellularization using the detergent sodium dodecyl sulfate (SDS). (A) Cross-section view shows the porous topography. Scale bar is 400 µm. (B) At higher magnification, the intricate network of interconnecting pores (yellow arrows) throughout the ECM is visible. Scale bar is 100 µm. (Adapted with permission from Reference 20.)

Figure 12.7 SEM images of porous scaffolds for cardiac tissue engineering. (A) PGS scaffolds were created by salt leaching. NaCl particles were incorporated in PGS polymer solution during polymerization then dissolved in water to leave 75- to 150-µm pores. Scanning electron micrographs reveal an extensive network of interconnected pores. Scale bar is 200 µm. (B) pHEMA-co-MAA hydrogel scaffold were fabricated using an array of rods PC as well as PMMA beads. After dissolution of the porogen, the network of interconnected 30-µm pores promoted angiogenesis, while the 60-µm diameter channels induced the formation of myocyte bundles. Scale bar is 100 µm. (C) Alginate sponges were made by freeze-drying a solution of cross-linked alginate. Scaffolds with 97-µm pores were modified with binding peptides to improve cell adhesion. Scale bar is 200 µm. (D) Anisotropic collagen–GAG scaffolds were fabricated using freeze-drying. To obtain elongated pores, the solution was frozen in a

Teflon cylinder between two copper plates. The arrow marks the scaffold's axis. Insert shows the best fit ellipse to the average pore shape. Scale bar is 200 µm. (Adapted with permission respectively from References 59, 61, 63, and 143.)

Figure 12.8 Electrospinning of anisotropic and multiscale scaffolds. Adult rat CMs were seeded on electrospun scaffolds of PLA that were (A) isotropic or (B) anisotropic due to being uniaxially stretched. Arrows in (A) show the filopodia-like structure that the cells create to spread on the scaffold while the arrow in (B) indicates the main fiber orientation that CMs follow. SEM images, scale bars are 40 µm. Another application of electrospinning is the fabrication of multiscale scaffolds. (C) Two solutions of polycaprolactone of different concentrations were electrospun simultaneously on the same collector to produce fibers with two mean diameters, 3.3 µm and 0.6 µm. Scale bars are 10 µm and 5 µm (insert). (D) SEM cross-sections show the ECM-like range of fiber diameters. Scale bar is 40 µm. (Adapted with permission from References 71 and 144.)

Figure 12.9 Alternatives to electrospinning to create micro- and nanofiber scaffolds. Rotary jet spinning uses a high-speed rotating spindle to draw fibers from synthetic and natural materials. (A) SEM images of gelatin fibers show a high degree of alignment. Surface-initiated assembly is a technique that mimics cell-mediated assembly and provides control of the scaffold nano- to macroscale structure and composition. (B) Schematic (left) and optical phase image (right) of two patterns of 20-µm width by 20-µm spacing fibronectin lines microcontact-printed orthogonally onto PIPAAm. After some time (ΔT) in cooling water, the mesh termed nanofabric is released and maintains its shape. (C) The same pattern was created with fibronectin (green) and laminin (red) and was released as a bicomponent nanofabric (right) showing that SIA can be used to control the architecture and composition of biomimetic ECM nanofabrics. (D) Three-dimensional, false-colored rendering of a fibronectin mesh with 20-μm wide elliptical holes observed by scanning electron microscopy. The nanofabric shows fishnet-like ripples. Scale bars are 40 μm in B and C and 100 μm for the released bicomponent nanofabrics. X, Y axes are 360 μm in D. (Adapted with permission from References 77 and 78.) *(See insert for color representation of the figure.)*

Figure 12.10 Examples of hydrogels for cardiac tissue engineering. Myocardial ECM gels can be obtained by decellularization, lyophilization, and enzymatic digestion. (A) The solubilized ECM components gel under physiological conditions into fibrous multicomponent hydrogels with ECM-like structure revealed by SEM. Scale bar is 1 μm. (B) Fibrin–matrigel hydrogels cast around an array of micropillars are remodeled by myocytes to form a contractile cardiac construct with local anisotropy. Scale bars are 500 μm (top) and 200 μm (bottom). (C) Synthetic polypeptides are designed to self-assemble into nanofibrous hydrogels and to mimic VEGF to induce angiogenesis. (Adapted with permission from References 89, 94, and 100.) *(See insert for color representation of the figure.)*

Figure 12.11 Microfabricated scaffolds for cardiac tissue engineering. (A) Design of PGS scaffolds laser-cut to create an accordion-like honeycomb structure. (B) The structural anisotropy of the scaffolds guided myocyte alignment, observed by immunostaining for F-actin (green) and nuclei (blue). 3-D printing can fabricate scaffolds layer by layer, with control over the microarchitecture. 2 × 2 cm 3-D-printed scaffolds with

(C) or without (D) ~1 mm pores can be seeded with cardiac progenitors. Scale bars are 200 μm in A and B, and the ruler is in centimeters in C and D. (Adapted with permission from References 18 and 107.)

Figure 12.12 Cell sheet engineering is a scaffold-free approach to cardiac tissue engineering. Human fibroblasts were seeded on an anisotropic PIPAAm layer. After release, the cell sheets produced their own anisotropic ECM, revealed by observation of highly aligned collagen type I fibers (green, left). Aligned cell sheets can be stacked at different angles to create multilayer constructs (right) with F-actin (red) and nuclei (blue). Scale bar is 100 μm. (Adapted with permission from Reference 110.) *(See insert for color representation of the figure.)*

Figure 12.13 Decellularization of whole rat hearts. (A) Photographs of cadaveric rat hearts before, during and after perfusion of SDS detergent over 12 hours (1% SDS in deionized water, 77.4 mmHg, 20°C); Ao, aorta; LA, left atrium; LV, left ventricle; RA, right atrium; RV, right ventricle. The RV, then the atria and the LV are cleared of cellular material, rendering the heart translucent. (B) H&E staining of decellularized heart showing leftover matrix and the complete absence of cells. Scale bar is 200 μm. The technique maintains large vasculature conduits (black asterisks). H&E, hematoxylin and eosin. (Adapted with permission from Reference 133.)

Figure 13.1 Schematic showing tissue engineering tools for controlling hierarchical structure, comprising of scaffolding techniques, bioreactors and biomolecules, and cell source manipulations.

Figure 13.2 Hierarchical organization of the cardiovascular system in the human body. This chapter focuses on the tissue engineering of the myocardium and the tunica media [8,205,256,257].

Figure 13.3 Schematic of making a master PDMS stamp with precise spatial cues using soft lithography. (Adapted from Kane *et al.* [85].)

Figure 13.4 Schematic of soft lithography techniques used to create micropatterning on substrates using (A) blocking methods and solution dispensing with microchannels or stencils, (B) microcontact printing of adsorbed proteins using conformal contact, and (C) affinity contact printing using immobilized ligands for conformal contact printing of target biomolecules. (Panel A adapted from Park and Shuler [136]; panel B adapted from Williams *et al.* [143,258]; panel C from Renault *et al.* [141].) *(See insert for color representation of the figure.)*

Figure 13.5 Cell sheet engineering technology using thermally responsive polymer poly(N-isopropylacrylamide) (P(NIPAAm)) allows cell attachment at 37°C and nonenzymatic cell detachment below lower critical solution temperature 32°C. Cell sheets can be harvested and layered in this manner. (Adapted from Elloumi-Hannachi *et al.* [259], Nakayama *et al.* [260], and Williams *et al.* [143].)

Figure 14.1 A reporter gene added to the DNA gene sequence produces a readily detectable fluorescent reporter protein, indicating that the functional promoter gene of interest has been expressed.

Figure 14.2 Under ultraviolet light, the bones of these transgenic mouse pups fluoresce green, indicating the successful incorporation of both the GFP reporter gene and the linked functional gene of interest. (Courtesy of Professor David Rowe of the University of Connecticut

Health Center.) *(See insert for color representation of the figure.)*

Figure 14.3 Transgenic mice are often developed from dark- and light-coated pairs to readily determine which of the offsprings contains the transgene. Shown here is the spotted chimeric mother and completely dark pups that are screened to be homozygous for the transgene. (Reprinted with permission from Reference 9.)

Figure 14.4 Fluorescence microscopy images of cultures expressing 3.6Col/GFP associated with preosteoblasts just prior to mineralization, and nontoxic xylenol orange (XO) staining of mineral taken from the same area in the cell culture plate at multiple time points. The cell reporter technology allows continuous monitoring of cell differentiation without requiring the use of dyes or antibody staining that require cell culture termination. (Courtesy of Yu-Hsiung Wang of the University of Connecticut Health Center.) *(See insert for color representation of the figure.)*

Figure 14.5 Scanning electron microscopy images of a carbonated hydroxyapatite coating at low and high magnification showing nanoscale, plate-like morphology. (A) Low mag. (100×) scale bar = 1 mm, (B) high mag. (5000×) scale bar = 20 μm.

Figure 14.6 To assess differences between test groups, the GFP-positive area (A) or the intensity (B) can be quantified and normalized to DNA content. In this study, the carbonated hydroxyapatite surface accelerated differentiation and mineralization of the osteoprogenitor cells compared to the TCPS control as evidenced by more GFP expression at an earlier time point. (Reprinted with permission from Reference 10.)

Figure 14.7 Fluorescence microscopy images of the calvarial cells from the transgenic mice on TCPS and cHA at 21 days with DAPI staining to show all cells (A,D), osteoblasts revealed by GFP expression (B,E), and XO staining for deposited mineral (C,F). Scale bar = 100 μm. (Reprinted with permission from Reference 10.) *(See insert for color representation of the figure.)*

Figure 14.8 Differences in morphology revealed by the fluorescence microscopy images allow distinction between the cHA substrate (A) without cells and (B) with cell-deposited mineral. Scale bar = 200 μm. (Reprinted with permission from Reference 10.)

Figure 14.9 Scanning electron micrograph (SEM) of fibrillar collagen surface. Scale bar = 30 μm.

Figure 14.10 Fluorescence microscopy images of GFP positive (green) and xylenol orange staining (red) of mineralized matrix after 14 and 21 days in culture. Scale bars = 2 mm. *(See insert for color representation of the figure.)*

Figure 14.11 Relative intensity of GFP and XO staining fluorescence images of the 14- and 21-day cultures measured by NIH ImageJ. The fibrillar collagen (FC) surface accelerated differentiation and mineralization at the earlier time point.

Figure 14.12 Merged fluorescence images showing colocalization of GFP expression and XO staining in cultures grown on nonfibrillar collagen (NFC). The inset image of XO staining shows isolated islands of mineral not associated with GFP positive differentiated cells. *(See insert for color representation of the figure.)*

Figure 15.1 Schematic drawings of cell-mediated matrix compaction for free-floating (top), uniaxially constrained (middle), and biaxially constrained (bottom) tissue equivalents. From an initial geometry (left), cells begin to spread and retract, resulting in matrix compaction that changes the overall geometry of the tissue equivalents (right).

Figure 15.2 General trend of radius reduction during cell-mediated compaction of a free-floating cell-populated lattice. During the *lag* phase, cells adhere to and begin to spread within the matrix. The *log* phase is characterized by a rapid reduction in the radius. Eventually, the lattice reaches a steady state when compaction ceases. The duration of each phase is dependent on many factors and can vary considerably depending on experimental protocol.

Figure 15.3 Picrosirius red stained free-floating fibroblast populated collagen lattice under circularly polarized light to show birefringent collagen. Central region (left) shows dense, randomly oriented collagen fibers while the outer edge of the lattice (right) shows aligned fibers for a lattice that has reached steady state (see Figure 15.2). Scale bar = 50 μm. *(See insert for color representation of the figure.)*

Figure 15.4 Example flow chart to implement a combined experimental–computational approach to study the mechanobiology of tissue equivalents.

Figure 16.1 Concepts of the HSC niche. (A) Scheme of HSC regulation inside the niche microenvironment depicting the different HSC fate decisions which are orchestrated by the niche components. (B) Scheme of the different microenvironmental cues controlling HSC fate including biochemical, biophysical, and metabolic signals. *(See insert for color representation of the figure.)*

Figure 16.2 Biomaterial approaches to mimic signals of niche microenvironment for control of stem cell fate. (A) Distinct options to present adhesion ligands or growth factors in microstructured biomaterials scaffolds for *in vitro* experiments allowing for one type of ligand and mixtures, gradients of ligands, as well as spatial control of presentation mode, for example, 2-D versus 2.5-D. (B) Varying the architecture of the biomaterials allows to mimic different morphological architectures of the niche microenvironment including open pores, fibrous substrates, and hydrogel entrapment. (C) Biomaterials mechanics can be modified to alter mechanotransduction pathways of stem cells including stiffness-dependent cell differentiation. (Inspired by Reference 39.)

Figure 16.3 Protein immobilization on a microstructured surface for HSC culture. (A) Poly(dimethyl siloxane) (PDMS) microstructured with oxygen plasma activation are coated by aminosilane functionalization and maleic anhydride copolymer coating to immobilize components of the ECM. (B) Fluorescent images of ECM-modified PDMS microstructures. *(See insert for color representation of the figure.)*

Figure 16.4 Synergistic action of adhesive micropatterns and soluble cytokines on HSC proliferation and differentiation. Single-cell microcavities at low cytokine levels maintain HSC in a quiescent and undifferentiated state. (A) Surface marker expression and cell number after 7 days of cell culture on fibronectin-coated microstructures. (B) Quantification of cell cycling by means of DNA synthesis (bromodeoxyuridine (BrdU) incorporation) directly on microstructures at low and high cytokine concentrations in the media. (C) Scheme of the balance of synergistic